UC Berkeley
UC Berkeley Previously Published Works

Title
Continental drift shifts tropical rainfall by altering radiation and ocean heat transport

Permalink
https://escholarship.org/uc/item/2q08s2c5

Journal
Science Advances, 9(10)

ISSN
2375-2548

Authors
Han, Jing
Nie, Ji
Hu, Yongyun
et al.

Publication Date
2023-03-10

DOI
10.1126/sciadv.adf7209

Peer reviewed

Continental drift shifts tropical rainfall by altering radiation and ocean heat transport

Jing Han[1], Ji Nie[1]*, Yongyun Hu[1]*, William R. Boos[2], Yonggang Liu[1], Jun Yang[1], Shuai Yuan[1], Xiang Li[1], Jiaqi Guo[1], Jiawenjing Lan[1], Qifan Lin[1], Xiujuan Bao[1], Mengyu Wei[1], Zhibo Li[1], Kai Man[1], Zihan Yin[1]

Shifts in the position of the intertropical convergence zone (ITCZ) have great importance for weather, climate, and society. The ITCZ shifts have been extensively studied in current and future warmer climate; however, little is known for its migration in the past on geological time scales. Using an ensemble of climate simulations over the past 540 million years, we show that ITCZ migrations are controlled primarily by continental configuration through two competing pathways: hemispheric radiation asymmetry and cross-equatorial ocean heat transport. The hemispheric asymmetry of absorbed solar radiation is produced mainly by land-ocean albedo contrast, which can be predicted using only the landmass distribution. The cross-equatorial ocean heat transport is strongly associated with the hemispheric asymmetry of surface wind stress, which is, in turn, controlled by the hemispheric asymmetry of ocean surface area. These results allow the influence of continental evolution on global ocean-atmosphere circulations to be understood through simple mechanisms that depend primarily on the latitudinal distribution of land.

INTRODUCTION

A narrow band of rainfall in the tropics, known as the intertropical convergence zone (ITCZ), encircles Earth's equator all year round. The ITCZ accounts for about one-third of global precipitation [e.g., (1)], and its annual mean latitude (ϕ_{ITCZ}) is about 4°N in the current climate (2, 3). The ITCZ plays an important role in Earth's weather and climate; for example, it modifies Earth's radiative balance and sensitivity to climate forcings (4). The variability of ϕ_{ITCZ} may notably affect the seasonal activity of tropical cyclones [e.g., (5)], and the persistent multiyear Sahel drought over the past century may be associated with decadal variability of the Atlantic ITCZ (6, 7).

The ITCZ is traditionally thought of as a tropical system that is mainly controlled by the distribution of tropical sea surface temperature [SST; e.g., (8)]. However, recent studies view the ITCZ as a meteorological equator that separates the atmospheric meridional mean circulations of the two hemispheres, closely linking ϕ_{ITCZ} and cross-equatorial atmospheric energy transport [e.g., (3, 9)]. This has provided greater recognition and understanding of how the position of the ITCZ may respond to a variety of both short- and long-term climate forcings and variabilities, such as glaciations (10), ocean heat transport variations (11), cloud changes (12), and aerosol and volcanic forcing (13–15). These advances have allowed the ITCZ to be used as an active indicator of various hemispheric asymmetries, especially for the large variations in climate that have occurred over thousands to many millions of years in the past [e.g., (2)].

Paleoclimate evidence has shown considerable migrations of the ITCZ that can be linked with externally forced climate changes or internal climate variability [e.g., (2, 3)]. For example, paleo records indicate that the ITCZ migrated northward through the early to mid-Holocene (8 to 6 ka ago) and retreated equatorward from mid- to late Holocene (6 ka ago to present) according to enhanced interhemispheric precession-induced insolation asymmetries (16, 17). During the last glacial period (~20 ka ago), clear millennial variation of ϕ_{ITCZ} associated with Heinrich stadials is seen in paleoclimate proxies (18, 19). Over longer time scales, we lack a clearly successful proxy for ITCZ position, but hints from paleoclimate simulations indicate substantial variations of the ITCZ [e.g., (20–22)]. Migration of the ITCZ in paleoclimate states is an interesting and important phenomenon unto itself, but it moreover has substantial implications because the ITCZ interacts with other components of the Earth system. For example, ITCZ position affects the location of equatorial cold water upwelling, which is crucial for ocean ecosystems and primary production [e.g., (23)]. The ITCZ position may also affect the chemical silicate-carbonate weathering rate over continents, which is critical in controlling Earth's CO_2 concentration on multimillion-year time scales [e.g., (24)].

This study has two goals. The first is to systematically examine the migration of the ITCZ position since the beginning of Phanerozoic with a series of time-slice simulations, which has not been done before. The simulations are performed with a comprehensive Earth system model using a synoptic scale–resolving resolution, from 540 Ma to the preindustrial (PI) period with a time interval of 10 Ma (fig. S1; see Materials and Methods for more details) (25). The results depict ITCZ variability over geological time scales: How far poleward did the ITCZ migrate, and what was the variability of ITCZ latitude? This ensemble of simulations over the past 540 Ma also details the characteristics of the tropical rainfall climatology in each geological period, which is valuable for paleoclimate, paleoecology, and paleogeology studies. The second goal, which is a major focus here, is to unveil the mechanism that

[1]Laboratory for Climate and Ocean-Atmosphere Studies, Department of Atmospheric and Oceanic Sciences, School of Physics, Peking University, Beijing, China. [2]Department of Earth and Planetary Science, University of California, Berkeley, Berkeley, CA, USA.
*Corresponding author. Email: jinie@pku.edu.cn (J.N.); yyhu@pku.edu.cn (Y.H.)

drives ITCZ migration on geological time scales. On these time scales, the main climate forcings external to the atmosphere-ocean system are changes of insolation, variations of greenhouse gases (mainly CO_2), and the evolution of continental configuration. In our experimental setting, the first two factors are highly hemispherically symmetric. Continental configuration, however, provides spatially inhomogeneous boundary conditions for geophysical fluid (ocean and atmosphere) motions that redistribute heat and greatly shape global and regional climates. We will show that migration of the ITCZ over geological time scales is largely driven by the continental evolution through two main pathways: the hemispheric asymmetry of radiation and ocean heat transport. Our results provide an atlas of paleoclimate states, deepen our understanding of ITCZ dynamics, and reveal an important relationship between paleoclimate and tectonic motion.

RESULTS
### Migration of the ITCZ
Annual-mean precipitation distributions of four representative periods are shown in Fig. 1 (continent configurations and precipitation distributions of all periods are in fig. S2 and movie S1). At 540 Ma, the supercontinent Pannotia had broken into Gondwana and several smaller continents (Fig. 1A). From 540 to 430 Ma, the smaller continents drifted across the equator, while the northern hemisphere (NH) rain belt extended longitudinally and the southern hemisphere (SH) rain belt contracted. Then, the continents slowly reassembled and formed the single supercontinent Pangea around 250 Ma (Fig. 1B). Beginning 170 Ma, Pangea broke up and drifted toward the North Pole. At around 80 Ma, the continental distribution was most fractured (Fig. 1C), partly because of

tectonic motions and sea level rise. Then, the continents slowly evolved to today's configuration (Fig. 1D), featured by the Atlantic expansion, the assembly of Eurasia, and the equatorward drift of Australia. The geographic distribution of tropical precipitation changed markedly with continental evolution. For example, the supercontinent Pangea was home to the intense rainfall zone on its eastern side, known as the Megamonsoon (20, 26); the formation of the South Pacific Convergence Zone accompanied the continental drift of Australia. However, in all periods, the global distribution of precipitation featured a broad tropical rain belt with a peak in each hemisphere (fig. S2), which is the subject of this study: the ITCZ.

Here, we focus on migrations of the annual- and zonal-mean ITCZ while leaving other features of the ITCZ, such as its seasonality, for future study. We quantify the ITCZ position using three quantities (see Materials and Methods): the latitude of the tropical precipitation centroid (ϕ_{ITCZ}), defined as the area-weighted mean latitude of zonal-mean precipitation from 20°S to 20°N [e.g., (27)]; the latitude of the tropical precipitation peak (ϕ_{pp}), defined as the latitude of the zonal-mean tropical precipitation maximum; and the precipitation asymmetry index (PAI), which quantifies the hemispheric asymmetry of tropical precipitation [e.g., (28, 29)]. Time series of these three parameters are shown in Fig. 2A, and the corresponding zonal-mean precipitation climatology are shown in fig. S3. The centroid, ϕ_{ITCZ}, shows relatively weak variability (ranging from 3°S to 4°N); the peak, ϕ_{pp}, shows large variability (9°S to 9°N) and sudden jumps between hemispheres, and the asymmetry index, PAI, varies from −0.3 (i.e., SH tropical precipitation is 30% stronger than NH tropical precipitation) to 0.36. Highlighting different aspects of the ITCZ, the three parameters are highly correlated. In the following, we mainly focus on ϕ_{ITCZ} for
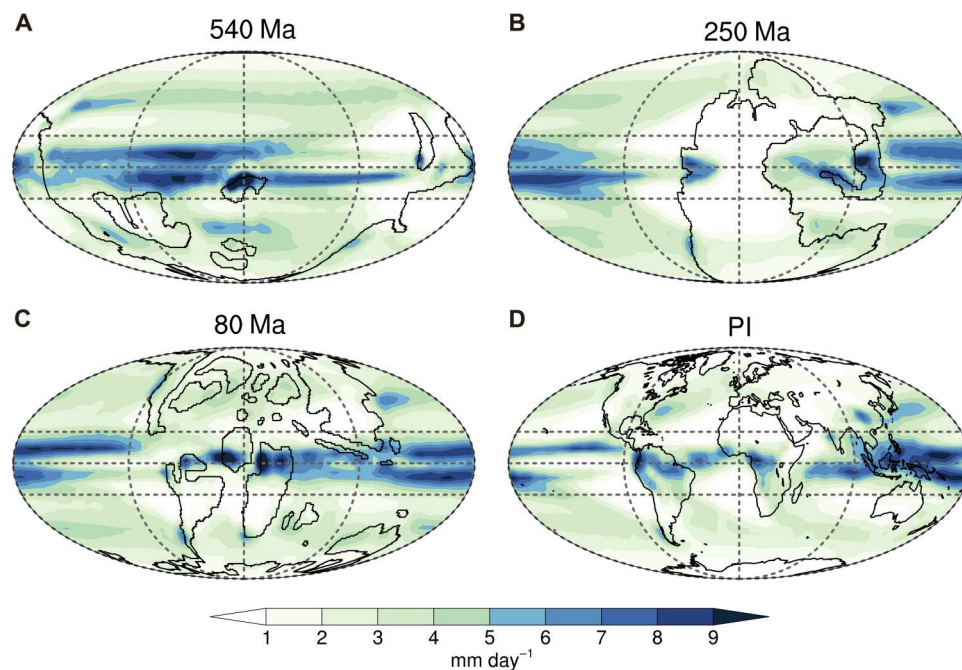
Fig. 1. Precipitation and continent configurations of four representative periods. The annual-mean precipitation (color, millimeter/day) and coastal lines (black lines) in the 540 Ma (**A**), 250 Ma (**B**), 80 Ma (**C**), and PI (**D**) simulations. The three horizontal dashed gray lines are the latitude grid lines of 20°N, equator, and 20°S from north to south, respectively. The vertical dashed gray lines are the longitude grid lines, whose spacing is 90°.
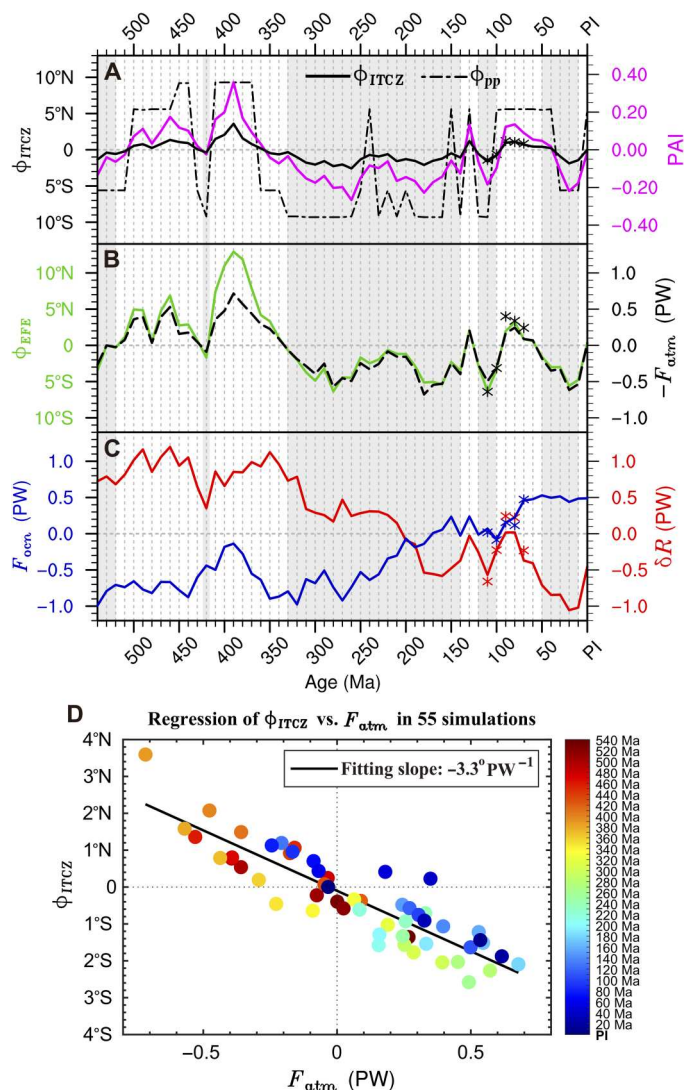
Fig. 2. ITCZ locations from the energetic perspective. (**A**) Time series of annual- and zonal-mean ϕ_{ITCZ}, ϕ_{pp}, and PAI. (**B**) Time series of ϕ_{EFE} (green line) and $-F_{atm}$ (black dashed line). (**C**) Time series of F_{ocn} (blue line) and δR (red line). The light and gray shading indicates the sign of F_{atm}. PW denotes petawatt. (**A** to **C**) The asterisks in each subplot show the results of the sensitive simulations with open drake passage during 110 to 70 Ma. (**D**) Scatter plot of ϕ_{ITCZ} versus F_{atm} in all the simulations (color dots). The black solid line is the linear-fitting line.

simplicity, keeping in mind that migrations of the ITCZ accompany systematic changes of atmospheric and oceanic circulations.

Aiming for a causal explanation of migrations of the ITCZ, we avoid linking the ITCZ position to internal climate variables, such as SST, because, then, one would need to answer the equally difficult question of what causes the SST changes in the simulations. Instead, we assess how ITCZ migrations are caused by changes in external parameters of the atmosphere-ocean climate system, such as concentrations of CO_2, insolation, and continental evolution (see Materials and Methods for how these are specified in the simulations).

To achieve our goal, we adopt an energetic framework [e.g., (3, 9)] to examine migrations of the ITCZ. Recognizing that the ITCZ is part of the rising branch of the time-mean tropical atmospheric

meridional overturning circulation, this framework posits that ϕ_{ITCZ} collocates with the latitude of the energy flux equator (ϕ_{EFE}), which is the tropical latitude with zero vertically integrated meridional atmospheric energy transport. If one applies a linear approximation to the meridional distribution of atmospheric energy transport near the equator and assumes the slope to be nearly invariant with climate state, then $-\phi_{EFE}$ is proportional to the cross-equatorial atmospheric energy transport (F_{atm}, positive values of which indicate northward transport). This energetic framework has been used to explain ITCZ variability from seasonal to millennial time scales [e.g., (2, 3, 27)]. Our simulations confirm the close correlation among ϕ_{ITCZ}, ϕ_{EFE}, and F_{atm} (Fig. 2, A and B, and fig. S4). The correlation between ϕ_{ITCZ} and ϕ_{EFE} is 0.89, and that between ϕ_{ITCZ} and $-F_{atm}$ is 0.89. The sensitivity of ϕ_{ITCZ} to F_{atm} is $-3.3°$ PW^{-1} (Fig. 2D), which agrees well with that found over the seasonal cycle and in externally forced annual averages in observations and coupled climate models (27). Furthermore, considering the energy balance of each hemisphere (fig. S5 and Materials and Methods), we may separate F_{atm} and, thus, ϕ_{ITCZ} into components associated with cross-equatorial ocean heat transport and the hemispheric asymmetry of radiation

$$\phi_{ITCZ} \propto -F_{atm} = F_{ocn} + \delta R \qquad (1)$$

Here, F_{ocn} is the ocean heat transport across the equator (positive denotes northward), and δR is the hemispheric asymmetry (NH minus SH) of net radiative energy input at the top of atmosphere (TOA). Equation 1 states that either a northward cross-equatorial ocean heat transport (F_{ocn}) or a positive net radiative heating asymmetry (δR) favors a NH ITCZ.

Now, we examine the time series of F_{ocn} and δR (Fig. 2C). From 540 Ma to present, F_{ocn} shows a clear trend from negative to positive with the sign changing around 170 Ma, superimposed with variations on shorter time scales. Conversely, δR has a negative trend of similar strength; thus, their sum F_{atm} shows no apparent linear trend over the whole time period. With the trend removed, F_{ocn} and δR show no apparent correlation (the correlation coefficient of the detrended time series is -0.38). Figure 2C also demonstrates that variations in F_{atm} are not dominated by either component; rather, F_{ocn} and δR are of equal importance and together produce the temporal variations of F_{atm} (fig. S6). The strong cancelation between F_{ocn} and δR is not a coincidence. In the following, we will examine the ocean heat transport and radiation asymmetry individually and argue that they are both caused by continental configuration changes over geological time scales.

Hemispheric asymmetry of radiation

The hemispheric asymmetry of radiation, δR, may be separated into a shortwave (δS, positive denotes inward energy) and longwave component (δL, positive denotes outgoing energy), respectively, so that $\delta R = \delta S - \delta L$ (Fig. 3, A and B). We find that δS dominates the variations in δR, with δL being much smaller. In addition, δL is anticorrelated with ϕ_{ITCZ} (Fig. 3B), consistent with high-level clouds and water vapor in the ITCZ trapping longwave radiation. Thus, δS variations may serve as a first-order approximation of δR variations.

Because annual-mean insolation is nearly hemispherically symmetric (the difference is less than 1 W m^{-2}), δS has to arise from the interhemispheric difference of planetary albedo. We hypothesize
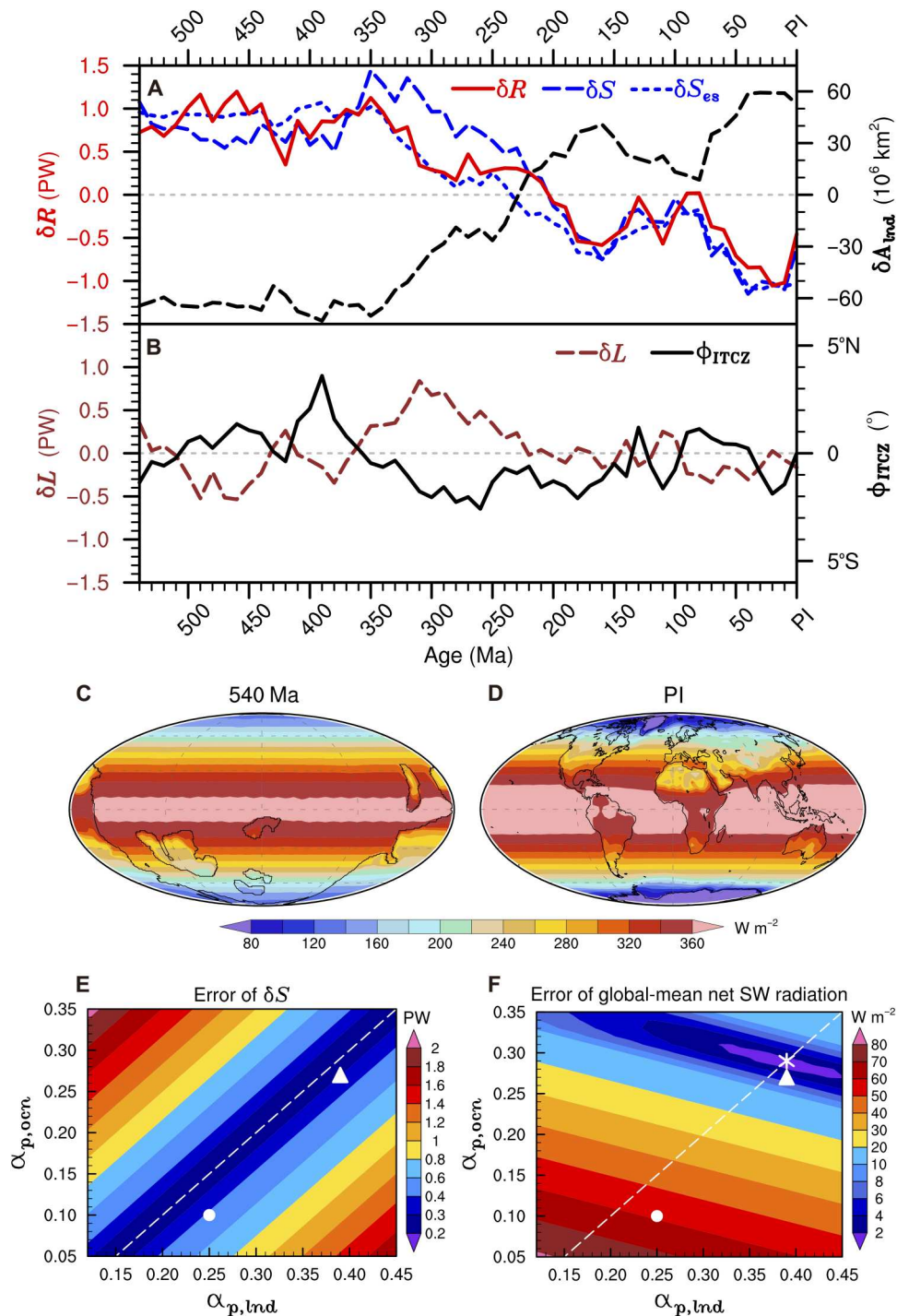
Fig. 3. The hemispheric asymmetry of radiations and related analyses. (**A**) δR, δS (the shortwave component of δR), δS_{es} (δS estimated by the simple model), and δA_{lnd}. (**B**) δL (the longwave component of δR) and ϕ_{ITCZ}. (**C** and **D**) Annual-mean TOA clear-sky net shortwave radiation (W m^{-2}) at 540 Ma and PI, respectively. (**E**) Mean absolute error between δS given by the simple model and the simulations. (**F**) Mean absolute error between global-mean net shortwave radiation given by the simple model and the simulations. The equations to calculate the errors are in Materials and Methods. The white dashed line indicates the minimum valley of the error in (E). The white asterisk in (F) is the optimal values of $\alpha_{p,\text{lnd}}$ and $\alpha_{p,\text{ocn}}$ for the simple model. The white triangles and dots in (E) and (F) indicate the global-mean all-sky and clear-sky planetary albedos over land and over ocean diagnosed from simulation outputs, respectively.

that variations in land-ocean albedo contrast dominate variations in the interhemispheric difference of planetary albedo. The clear-sky net shortwave radiation at the TOA shows that land reflects more solar radiation than ocean [Fig. 3 (C and D) shows two representative periods, and fig. S7 shows all periods]; clouds also affect planetary albedo, but we show later that they make little contribution to variations in the hemispheric asymmetry of radiation.

On the basis of these results, we construct a simple model of δS using only the landmass distribution. We simplify the planetary albedos over land and ocean as uniform (spatially and temporally over different geological periods) values of $\alpha_{p,lnd}$ and $\alpha_{p,ocn}$, respectively. For each location, given its annual-mean insolation, we can calculate its local TOA net shortwave radiation depending on whether it is over land or ocean surface. Integrating it over each hemisphere, we have the net shortwave radiation of each hemisphere (see Materials and Methods) and, thus, its hemispherical asymmetry (δS_{es}, the subscript denotes values estimated by the simple model).

We compare the calculation of the simple model to the simulation results to determine the coefficients of $\alpha_{p,lnd}$ and $\alpha_{p,ocn}$. With each possible pair of $\alpha_{p,lnd}$ and $\alpha_{p,ocn}$, we calculate the corresponding δS_{es} for each time period. The performance of the simple model may be estimated by the mean absolute difference between δS_{es} and the simulated δS by the Earth system model (see Materials and Methods). The discrepancy between δS_{es} and δS is minimized with a land-ocean albedo contrast of 0.1 ($\alpha_{p,lnd} - \alpha_{p,ocn} = 0.1$, corresponding to the white dashed line in Fig. 3E), with little constraint on the absolute values of either albedo. This suggests that land-ocean albedo contrast is the main cause of δS. We may further constrain $\alpha_{p,lnd}$ and $\alpha_{p,ocn}$ by comparing the simple model–estimated and simulated global mean net shortwave radiation at the TOA (Fig. 3F), yielding the optimal values of $\alpha_{p,lnd} = 0.39$ and $\alpha_{p,ocn} = 0.29$ (the asterisk in Fig. 3F). These values are close to both observed estimates in modern climate [e.g., (30)] and mean values diagnosed from all our simulations (the white triangle in Fig. 3F). Figure 3A shows that variations in δS_{es} estimated using these optimized albedos are very close to variations in δS and δR, with correlation coefficients of 0.90 and 0.96, respectively. Given the robustness of the parameters over geological time and the accuracy of the simple model, we speculate that it may be applied in other paleoclimate periods.

The dominant role of land-ocean albedo contrast in controlling δS is further demonstrated by additional lines of evidence. First, we note that the values of $\alpha_{p,lnd}$ and $\alpha_{p,ocn}$ obtained above represent planetary albedos (estimated at TOA), including effects of the atmosphere and surface. The atmosphere affects planetary albedo through absorption, scattering, and reflection of shortwave in clear and cloudy skies. Observational studies of modern climate indicate that the atmosphere contributes more to planetary albedo than the surface [e.g., (31, 32)]. Thus, we expect the contrast between $\alpha_{p,lnd}$ and $\alpha_{p,ocn}$ to be smaller than the contrast between the surface albedos of land and ocean (typical values are 0.26 and 0.05, respectively) (33), as is true of our estimated planetary albedos. Examining the effects of clear-sky and cloud processes on the hemispheric asymmetry of radiation, we find that the clear-sky component of the asymmetry dominates (fig. S8). The clear-sky planetary albedos over land and ocean diagnosed in our simulations (the white dots in Fig. 3, E and F) are smaller than the all-sky planetary albedos [the white triangles in Fig. 3 (E and F)], so using them in the

simple model would overestimate global mean net shortwave radiation (Fig. 3F). However, even those clear-sky values reproduce δS_{es} well (Fig. 3E), highlighting the dominant role of land-ocean albedo contrast rather than the absolute values of albedos. Furthermore, there is strong cancelation between the longwave and shortwave effects of clouds on δR (fig. S8). Thus, while clouds play important roles in local and global-mean radiative balances, they seem to have little contribution to variations in the hemispheric asymmetry of radiation driven by continental drift.

Last, although the latitude of landmasses is part of the input parameters in the simple model, δS_{es} is mainly determined by the hemispheric difference in land area (δA_{lnd}), as shown by the strong anticorrelation between δS_{es} and δA_{lnd} (Fig. 3A).

In summary, these results indicate that over geological time scales, land-ocean albedo contrast largely determines δR. Using only the horizontal distribution of land (and no information on surface type or orography), we can well estimate δR. This link between δR and continental configuration constitutes the first pathway for how continental evolution affects migrations of the ITCZ.

Ocean heat transport

Now, we examine the ocean heat transport, which, in our simulations, exerts an opposite influence on ITCZ migration compared with that of the hemispheric asymmetry of radiation. The cross-equatorial ocean heat transport plays an important role in setting the latitude of the ITCZ in the current climate (3, 11, 34) and is dominated by the deep global meridional overturning circulation (GMOC) of the ocean (35). This GMOC is clockwise (defined as northward at upper levels), mostly because of the Atlantic overturning circulation (36). Cold and salty water sinks into the deep ocean in the North Atlantic, while the strong SH surface westerlies bring deep water to the ocean surface by Ekman pumping within the polar part of the Antarctic Circumpolar Current (ACC) (37, 38). The clockwise GMOC transports heat from the SH to the NH and pins the ITCZ north of the equator. The even deeper overturning circulation associated with the deep-water formation around the Antarctica has a negligible contribution to heat transport (39). Such bottom overturning circulation, if it exists, also has negligible contribution to ocean heat transport in all the simulated previous climates due to the small temperature difference between its upper and lower branches and is thus ignored and not counted in the GMOC in the context herein.

Consistent with the time series of F_{ocn} (Fig. 2C), our simulations show an anticlockwise GMOC (interhemispheric in almost all cases) before 170 Ma and a clockwise GMOC after 90 Ma, with oscillations in direction during the transition period (160 to 100 Ma; fig. S9). The dynamics of GMOC is a complicated, unsettled topic of great importance (40, 41); it is out of our scope to provide a theory for the GMOC here. Instead, we boldly propose, on the basis of the simulation results, that for variability over geological time, the direction of the GMOC is mainly set by the hemispheric asymmetry of area-integrated wind stress on the ocean surface, especially in the middle latitudes. This assertion is supported by the strong anticorrelation (a coefficient of -0.86; Fig. 4A) between F_{ocn} and the hemispheric asymmetry of wind stress $\delta\langle\tau\rangle$, defined as area-integrated wind stress over the ocean surface and normalized by hemispheric area in the NH minus that in SH (see Materials and Methods).
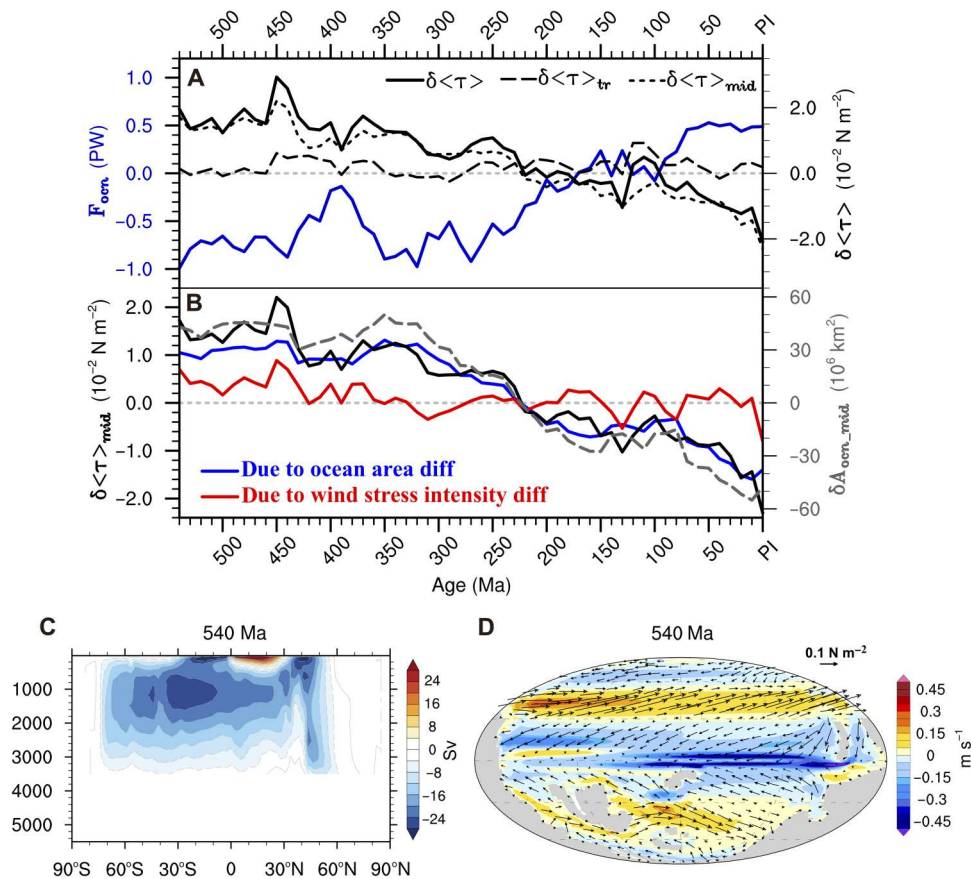
Fig. 4. The cross-equatorial ocean heat transport and related analyses. (**A**) F_{ocn} (blue line), $\delta\langle\tau\rangle$, and its components in the tropics ($\delta\langle\tau\rangle_{tr}$) and mid-latitudes ($\delta\langle\tau\rangle_{mid}$). (**B**) $\delta\langle\tau\rangle_{mid}$ (black line) and its decompositions due to hemispheric differences of ocean surface area (blue line) and wind stress intensity (red line). The gray dashed line shows δA_{ocn_mid}. (**C**) Mass streamfunction of GMOC [with units of sverdrup (Sv)] at 540 Ma. The red (blue) color corresponds to a clockwise (anticlockwise) circulation. (**D**) Ocean surface wind stress (vector, unit: N m^{-2}) and ocean surface zonal current (color, unit: m s^{-1}) at 540 Ma. Warm (cold) colors denote the eastward (westward) flow.

Prior studies based on seasonal to interannual variability of the modern ITCZ suggested that cross-equatorial ocean heat transport is dominated by the ocean's shallow tropical circulation cells [e.g., (*42–44*)]. These studies argued that the trade winds exert stress on the tropical ocean, which, because of Sverdrup balance, couple the tropical shallow ocean cells with the tropical Hadley cell. However, decomposition of $\delta\langle\tau\rangle$ (Fig. 4A) shows that its variations due to tropical components (within 30°N/S) are close to zero, while its mid-latitude (30° to 70° in each hemisphere) component dominates. The component of $\delta\langle\tau\rangle$ in the polar region is even smaller. This indicates that for ITCZ variability over geological time scales, the cross-equatorial ocean heat transport is determined by ocean deep overturning circulations driven by surface westerlies in middle latitudes rather than by tropical shallow cells driven by tropical winds.

Examining wind stresses (fig. S10) and the GMOC (fig. S9) in all the simulations confirms their strong relationship. Taking the 540-Ma period as an example (Fig. 4, C and D), when landmasses are concentrated in the SH and the NH is a vast open ocean, there is a strong NH mid-latitude surface ocean current (Fig. 4D), which may be analogous to the ACC in the present climate (although in the opposite hemisphere). This mid-latitude current is accompanied by deep-water upwelling (Fig. 4C) due to Ekman transport

and Ekman pumping induced by the wind stress and its curl and an anticlockwise GMOC. A similar relationship is found in other periods, such that the hemisphere with a wider ocean and stronger westerly winds in the mid-latitude is often the hemisphere with the rising branch of the GMOC (fig. S9 and S10). The wind-driven adiabatic component of the GMOCs dominates the diabatic component driven by vertical eddy diffusion (*40*) in most periods, as inferred from the larger number of streamlines rising within the westerlies-driven upwelling zones than in other regions (fig. S9). This dominance of the adiabatic GMOC is consistent with the good relationship between F_{ocn} and $\delta\langle\tau\rangle$. This relationship is also consistent with zonal-mean theory that, for the present-day Earth, treats the net northward flux of ocean water by Ekman transport across the northern boundary of the ACC as a cause of the strength of the GMOC (the adiabatic part) (*45*).

Because the mid-latitude component $\delta\langle\tau\rangle_{mid}$ dominates the total wind stress asymmetry $\delta\langle\tau\rangle$, we further decompose $\delta\langle\tau\rangle_{mid}$ into components due to hemispheric differences in mid-latitude ocean surface area (δA_{ocn_mid}) and due to hemispheric differences in mid-latitude wind stress intensity (see Materials and Methods). The component due to δA_{ocn_mid}, which is a geographic parameter, explains most of the variability of $\delta\langle\tau\rangle_{mid}$, while the component due to hemispheric differences in wind stress intensity is secondary
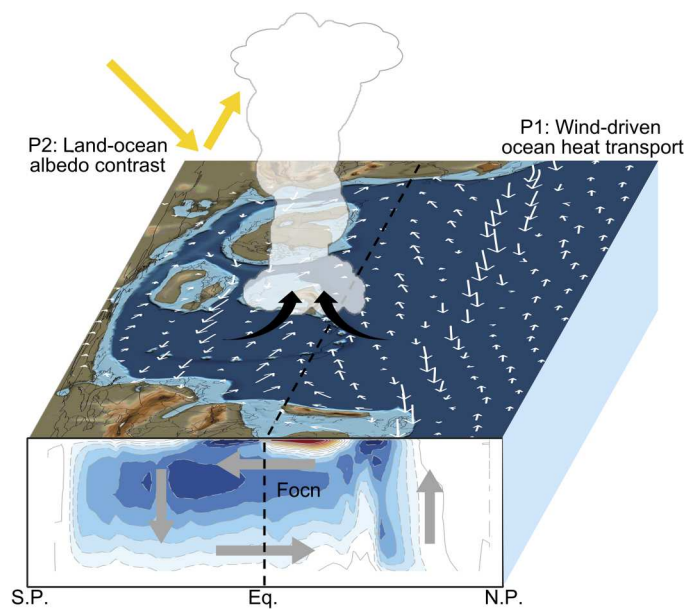
Fig. 5. Schematic of the two pathways of continental evolution driving the migration of ITCZ. Wind-driven ocean heat transport and land-ocean albedo contrast. The situation at 540 Ma is plotted for illustration, showing continental distribution, the ocean surface wind stress (white arrows), the ocean circulation (stream function and gray arrows at the bottom), and the ITCZ.

(Fig. 4B). This partition may be expected because the variability of $\delta A_{\text{ocn\_mid}}$ due to continental drift over the examined time period is significantly larger than the variability of asymmetry of wind stress intensity. As a result, there is a very strong correlation (a coefficient of -0.91) between F_{ocn} and $\delta A_{\text{ocn\_mid}}$. The greater importance of ocean area compared to wind stress intensity may allow for more faithful representation of climate in Earth system models because the GMOC in low-resolution models tends to be too sensitive to changes in wind stress (*46*); the dependence of F_{ocn} on $\delta \langle \tau \rangle$ in our simulations is furthermore not due to a spurious sensitivity of the modeled GMOC to wind stress intensity. The results here do not argue against the roles of buoyance forcing in ocean dynamics, which is apparently important in setting the detailed structure of the GMOC (*47*). However, among the simulations, the hemispheric difference of buoyancy forcing is arguably much smaller than the hemispheric difference of wind stress, and the buoyancy forcing is less deterministic in setting the direction of ocean circulation (*47*). In summary, the above analysis indicates that F_{ocn} is mainly set by the hemispheric asymmetry of mid-latitude ocean surface area due to the cross-equatorial ocean heat transport associated with the wind-driven GMOC.

Last, let us put the arguments made in the above two sections together. If we estimate δR by the simple model of radiation asymmetry and F_{ocn} by a linear fitting using $\delta A_{\text{ocn\_mid}}$, the estimated F_{atm} follows the simulated F_{atm} reasonably well (fig. S11), especially for the longer time scale variability, albeit there are sizeable discrepancies in shorter time scales. Given that the only input for the above estimation is continental configurations (with coefficients retrieved by fitting simulations), this match further highlights the strong explanatory power of the simple arguments.

DISCUSSION

Using a series of climate simulations, this study shows that over geological time (540 Ma to present), migrations of the zonal-mean tropical rain belt may be attributed to changes in size and latitude of continents. The continental configuration sets ITCZ latitude through two main pathways: cross-equatorial ocean heat transport and hemispheric asymmetry of radiation (see the schematic in Fig. 5). The hemisphere with larger mid-latitude ocean area has a stronger wind stress–forced upwelling and equatorward Ekman transport, resulting in an ocean MOC that transports heat toward the opposite hemisphere. On the other hand, the hemisphere with smaller land area has a lower planetary albedo, thus absorbing more solar radiation. These two mechanisms have competing effects on the ITCZ, and the cross-equatorial atmospheric energy flux required to balance their residual explains the migration of the ITCZ from the perspective of continental evolution.

Although our simulations and analyses reveal the first-order mechanisms of geological time-scale migrations of the zonal-mean ITCZ, we used simplifications and other factors that merit exploration in future work. Here, the ITCZ latitude was linked only to bulk parameters of continental configuration; including additional parameters such as orography or land surface type may improve our prediction. Given that our simple estimate of δR is quite accurate (Fig. 3A) while the correlation between $\delta A_{\text{ocn\_mid}}$ and F_{ocn} is weaker (Fig. 4, A and B), the space for improvement lies in a better understanding of the dependence of ocean circulation on continental configuration. Previous studies [e.g., (*48–51*)] have shown that continental changes in key areas (e.g., formation of the Isthmus of Panama and uplift of the Tibetan plateau) may affect the ocean general circulation and tropical rainfall. Motivated by that work, we carried out a set of sensitivity tests, keeping the same settings as the control cases except for opening the Drake passage during the period of 110 to 70 Ma. The results [asterisks in Fig. 2 (A to C)] show that the perturbations to ϕ_{ITCZ} are relatively small compared with those due to continental evolution over geological time. Our conclusions thus seem to not to be affected much by the state of the Drake passage, but this issue deserves further study.

The latitude of the zonal-mean ITCZ serves as an indicator of a broad variety of hemispheric asymmetries and has profound implications for global weather and climate. For example, in the current climate, the NH summer monsoons are significantly stronger than their SH counterparts (*52*), which is associated with the annual-mean ITCZ lying north of the equator. Currently, the SH is much stormier than the NH, and Shaw *et al.* (*53*) attribute this to hemispheric asymmetry in an energy framework of similar philosophy to that used here. Thus, our results motivate further study of the hemispheric asymmetry of other weather and climate components, their evolution over geological time, and their linkage with geographic parameters.

MATERIALS AND METHODS
Numerical model and experimental design
The experiment setting follows that by Li *et al.* (*25*). Li *et al.* (*25*) includes a set of low-resolution atmosphere-ocean coupled simulations and a set of high-resolution atmosphere-only simulations and mainly show the results of the high-resolution experiments. Here,

we use the low-resolution coupled simulations because interactive ocean is critical in driving ITCZ. Here, we only briefly describe the experiment setting, while the details can be found in the work of Li *et al.* (*25*).

The Community Earth System Model [CESM1.2.2; (*54*)] is used here. It simulates the processes within and interactions among the atmosphere, ocean, land, sea ice, and river runoff. The horizontal resolutions are 3.75° × 3.75° for the atmosphere and land and g37 (116 meridional grids and 100 zonal grids) for the dynamic ocean and sea ice, respectively. There are 26 vertical levels for the atmosphere and 60 vertical levels for the ocean.

We carry out a series of time-slice simulations from 540 to 10 Ma with an interval of 10 Ma, as well as the PI climate. The simulated time period is chosen largely to be consistent with the set of reconstructed paleogeographic (*55*). For the PI case, the CO_2, CH_4, and N_2O are uniformly distributed with concentrations of 280 parts per million by volume (ppmv), 760 parts per billion by volume (ppbv), and 270 ppbv, respectively. The simulation of the PI matches with the observations reasonably well (figs. S2 and S3). The main differences among the paleoclimate simulations are the continental configurations and the global mean temperature. The paleogeographic maps, which include the elevation of the land surface and bathymetric configuration, are from the paleo-digital elevation model (paleoDEM) (*55*). For each simulation, the CO_2 concentration is tuned to match the reconstructed global mean surface temperatures (*56*, *57*) in the corresponding time period. This approach ensures a good match with the targeting global mean surface temperature; however, the cost is that the applied CO_2 concentration is notably higher than those from proxy reconstruction [e.g., figure 5 in (*25*)] at certain time periods. Considering the increases of luminosity of the Sun over time, insolation is linearly increased from 1302 Wm^{-2} at 540 Ma to 1361 Wm^{-2} at present (*58*). All other atmospheric compositions and the orbital parameters are set to the PI values. Each simulation is run into its equilibrium state (after more than 5000 model years, with the net radiation at the TOA less than 0.1 Wm^{-2}), and the last 100 years' outputs are analyzed.

Observational data
For the validation of the PI simulation, the following observational data are used: Global Precipitation Climatology Project (GPCP2.3) (*59*) data and the fifth generation of European Centre for Medium-Range Weather Forecasts reanalysis data (ERA5) (*60*), between 1981 and 2010.

Energetic framework of ITCZ
We use three quantities to depict the migration of the ITCZ. The first one is ϕ_{ITCZ}, which is the latitude of tropical precipitation centroid between 20°S and 20°N [e.g., (*27*)]. The second one is ϕ_{PP}, which is the latitude of the zonally averaged tropical precipitation maximum. The third one is the PAI [e.g., (*28*, *29*)], which quantifies the tropical hemispheric asymmetry of precipitation and calculated as $\mathrm{PAI} = \frac{\int_0^{20°N} P\cos(\phi)d\phi - \int_{20°S}^0 P\cos(\phi)d\phi}{\int_{20°S}^{20°N} P\cos(\phi)d\phi}$ in which P is the annual- and zonal-mean precipitation and ϕ is the latitude.

The energetic framework [e.g., (*3*, *9*)] is built on the basis that the ITCZ lies near the energy flux equator (ϕ_{EFE}), which may be further related with the cross-equatorial atmospheric energy (the sum of sensible, latent, and geopotential energy fluxes) transport (F_{atm}),

by a linear approximation so that $\phi_{ITCZ} \approx \phi_{EFE} \approx -\frac{1}{a}\frac{F_{atm}}{NEI_0}$, where a is the radius of Earth and NEI_0 is the atmospheric net energy input at the equator. We have examined that in our simulations, the variability of ϕ_{EFE} is mostly due to the variability of F_{atm}, while NEI_0 may be taken as a constant (i.e., the averaged NEI_0 of all the simulations; fig. S4).

Next, we consider the energy balance of each hemisphere. In an equilibrium state, the net energy inputted into one hemisphere at the TOA has to be transported out by its lateral boundaries at the equator by atmosphere and ocean (see the schematic in fig. S5). Let R_{NH} and R_{SH} be the net radiative energy input of NH and SH (units of Watt, positive denotes energy input) and F_{atm} and F_{ocn} be the cross-equatorial atmospheric and oceanic energy transports (positive denotes northward), respectively; we have $R_{SH} = F_{ocn} + F_{atm}$ and $R_{NH} = -(F_{ocn} + F_{atm})$. Then, we may define a hemispheric asymmetry of net radiative heating $\delta R = (R_{NH} - R_{SH})/2$ in which δ denotes the difference between the NH and SH hereafter. Thus, we have $-F_{atm} = F_{ocn} + \delta R$, which is Eq. 1.

A simple model of the hemispheric asymmetry of radiation
For the simple model of the hemispheric asymmetry of radiation, we assume that the planetary albedos over land and ocean are constants ($\alpha_{p,lnd}$ and $\alpha_{p,ocn}$, respectively). The TOA net shortwave heating over a unit area, with its annual-mean insolation (I), is $I(1 - \alpha_{p,lnd})$ or $I(1 - \alpha_{p,ocn})$, depending on its surface type. Then, given an arbitrary landmass distribution, the net shortwave radiation at TOA averaged over the NH can be calculated as $S_{NH} = \int_{lnd,NH} I(1 - \alpha_{p,lnd})ds + \int_{ocn,NH} I(1 - \alpha_{p,ocn})ds$, where the two integrals are applied over the NH land and ocean areas, respectively. The SH net shortwave radiation, S_{SH}, can be calculated similarly. Then, the simple model–estimated hemispheric asymmetry of net shortwave radiation is $\delta S_{es} = (S_{NH} - S_{SH})/2$. To quantify the performance of the simple model, we calculate the absolute mean error (i.e., cost function) by comparing the results from the simple model with the results from the numerical simulations as $\varepsilon = \frac{1}{55}\sum_{i=1}^{55} |\delta S_{es,i} - \delta S_i|$, in which the subscript i denotes results of each geological time period. ε is shown in Fig. 3E for a range of combinations of $\alpha_{p,lnd}$ and $\alpha_{p,ocn}$. Similarly, we can use the simple model to calculate the global averaged net shortwave radiation $S_{glb,es} = (S_{NH} + S_{SH})/(2A_0)$ (with units of W m^{-2}) in which A_0 is the hemisphere area (255×10^6 km^2). Again, the error of this quantity from the simple model compared with the simulation results is $\varepsilon = \frac{1}{55}\sum_{i=1}^{55} |S_{glb,es,i} - S_{glb,i}|$ as shown in Fig. 3F.

Calculation of the ocean wind stress intensity
We areally average the wind stress intensity (τ, with units of N m^{-2}) over oceans of each hemisphere, and their difference is thus $\delta\langle\tau\rangle = \frac{1}{A_0}(\langle\tau\rangle_N - \langle\tau\rangle_S) = \frac{1}{A_0}(\int_{A_{ocn,N}} \tau_N ds - \int_{A_{ocn,S}} \tau_S ds)$. $A_{ocn,N}$ and $A_{ocn,S}$ denotes the ocean area of the NH and SH, respectively, and A_0 is hemisphere area. $\delta\langle\tau\rangle$ may be further decomposed into components due to hemispheric differences of ocean area and hemispheric differences of wind stress intensity. We first define a mean wind stress intensity $\overline{\tau}$ in each hemisphere so that $\delta\langle\tau\rangle \approx \frac{1}{A_0}(\overline{\tau_N}A_{ocn,N} - \overline{\tau_S}A_{ocn,S})$ and then let $\overline{\tau_G} = \frac{1}{2}(\overline{\tau_N} + \overline{\tau_S})$ and $\delta\overline{\tau} = (\overline{\tau_N} - \overline{\tau_S})/2$, so we have $\delta\langle\tau\rangle \approx \frac{1}{A_0}[\overline{\tau_G}\delta A_{ocn} + \delta\overline{\tau}(A_{ocn,N} + A_{ocn,S})]$, where $\delta A_{ocn} = A_{ocn,N} -$

$A_{\text{ocn},S}$. The right-hand-side terms in the brackets are components due to hemispheric differences of ocean area and wind stress intensity, respectively. The above decomposition may be applied for the tropical or mid-latitude component of $\delta\langle\tau\rangle$ individually.

Supplementary Materials
This PDF file includes:
Figs. S1 to S11
Legend for movie S1

Other Supplementary Material for this manuscript includes the following:
Movie S1

REFERENCES AND NOTES

1. S. M. Kang, Y. Shin, S.-P. Xie, Extratropical forcing and tropical rainfall distribution: Energetics framework and ocean Ekman advection. *npj Clim. Atmos. Sci.* **1**, 20172 (2018).

2. J. C. H. Chiang, A. R. Friedman, Extratropical cooling, interhemispheric thermal gradients, and tropical climate change. *Annu. Rev. Earth Planet. Sci.* **40**, 383–412 (2012).

3. T. Schneider, T. Bischoff, G. H. Haug, Migrations and dynamics of the intertropical convergence zone. *Nature* **513**, 45–53 (2014).

4. S. Bony, B. Stevens, D. Coppin, T. Becker, K. A. Reed, A. Voigt, B. Medeiros, Thermodynamic control of anvil cloud amount. *Proc. Natl. Acad. Sci. U.S.A.* **113**, 8927–8932 (2016).

5. G. Zhang, Z. Wang, Interannual variability of the Atlantic Hadley Circulation in boreal summer and its impacts on tropical cyclone activity. *J. Climate* **26**, 8529–8544 (2013).

6. C. K. Folland, T. N. Palmer, D. E. Parker, Sahel rainfall and worldwide sea temperatures, 1901–85. *Nature* **320**, 602–607 (1986).

7. D. W. J. Thompson, J. M. Wallace, J. J. Kennedy, P. D. Jones, An abrupt drop in Northern Hemisphere sea surface temperature around 1970. *Nature* **467**, 444–447 (2010).

8. S.-P. Xie, The shape of continents, air–sea interaction, and the rising branch of the Hadley circulation, in *The Hadley Circulation: Present, Past, and Future*, H. F. Diaz, R. S. Bradley, Eds. (Springer Science & Business Media, 2004), pp. 121–152.

9. S. M. Kang, I. M. Held, D. M. W. Frierson, M. Zhao, The response of the ITCZ to extratropical thermal forcing: Idealized slab-ocean experiments with a GCM. *J. Climate* **21**, 3521–3532 (2008).

10. D. W. Lea, D. K. Pak, L. C. Peterson, K. A. Hughen, Synchroneity of tropical and high-latitude Atlantic temperatures over the last glacial termination. *Science* **301**, 1361–1364 (2003).

11. D. M. W. Frierson, Y.-T. Hwang, N. S. Fučkar, R. Seager, S. M. Kang, A. Donohoe, E. A. Maroon, X.-J. Liu, D. S. Battisti, Contribution of ocean overturning circulation to tropical rainfall peak in the Northern Hemisphere. *Nat. Geosci.* **6**, 940–944 (2013).

12. S. M. Kang, D. M. W. Frierson, I. M. Held, The tropical response to extratropical thermal forcing in an idealized GCM: The importance of radiative feedbacks and convective parameterization. *J. Atmos. Sci.* **66**, 2812–2827 (2009).

13. M. Zuo, T. Zhou, W. Man, Hydroclimate responses over global monsoon regions following volcanic eruptions at different latitudes. *J. Climate* **32**, 4367–4385 (2019).

14. T. W. Jacobson, W. Yang, G. A. Vecchi, L. W. Horowitz, Impact of volcanic aerosol hemispheric symmetry on Sahel rainfall. *Clim. Dyn.* **55**, 1733–1758 (2020).

15. R. D'Agostino, C. Timmreck, Sensitivity of regional monsoons to idealised equatorial volcanic eruption of different sulfur emission strengths. *Environ. Res. Lett.* **17**, 054001 (2022).

16. G. H. Haug, K. A. Hughen, D. M. Sigman, L. C. Peterson, U. Röhl, Southward migration of the Intertropical Convergence Zone through the Holocene. *Science* **293**, 1304–1308 (2001).

17. W. Boos, R. Korty, Regional energy budget control of the intertropical convergence zone and application to mid-Holocene rainfall. *Nat. Geosci.* **9**, 892–897 (2016).

18. X.-F. Wang, A. S. Auler, R. L. Edwards, H. Cheng, P. S. Cristalli, P. L. Smart, D. A. Richards, C.-C. Shen, Wet periods in northeastern Brazil over the past 210 kyr linked to distant climate anomalies. *Nature* **432**, 740–743 (2004).

19. E. W. Wolff, J. Chappellaz, T. Blunier, S. O. Rasmussen, A. Svensson, Millennial-scale variability during the last glacial: The ice core record. *Quat. Sci. Rev.* **29**, 2828–2838 (2010).

20. J. E. Kutzbach, R. G. Gallimore, Pangaean climates: Megamonsoons of the megacontinent. *J. Geophys. Res.* **94**, 3341–3357 (1989).

21. G. Ramstein, F. Fluteau, J. Besse, S. Joussaume, Effect of orogeny, plate motion and land–sea distribution on Eurasian climate change over the past 30 million years. *Nature* **386**, 788–795 (1997).

22. A. Farnsworth, D. J. Lunt, S. A. Robinson, P. J. Valdes, W. H. G. Roberts, P. D. Clift, P. Markwick, T. Su, N. Wrobel, F. Bragg, S.-J. Kelland, R. D. Pancost, Past East Asian monsoon evolution controlled by paleogeography, not CO_2. *Sci. Adv.* **5**, eaax1697 (2019).

23. G. T. Taylor, F. E. Muller-Karger, R. C. Thunell, M. I. Scranton, Y. Astor, R. Varela, L. T. Ghinaglia, L. Lorenzoni, K. A. Fanning, S. Hameed, O. Doherty, Ecosystem responses in the southern Caribbean Sea to global climate change. *Proc. Natl. Acad. Sci. U.S.A.* **109**, 19315–19320 (2012).

24. F. A. Macdonald, N. L. Swanson-Hysell, Y. Park, L. Lisiecki, O. Jagoutz, Arc-continent collisions in the tropics set Earth's climate state. *Science* **364**, 181–184 (2019).

25. X. Li, Y. Hu, J. Guo, J. Lan, Q. Lin, X. Bao, S. Yuan, M. Wei, Z. Li, K. Man, Z. Yin, J. Han, J. Zhang, C. Zhu, Z. Zhao, Y. Liu, J. Yang, J. Nie, A high-resolution climate simulation dataset for the past 540 million years. *Sci. Data* **9**, 371 (2022).

26. J. T. Parrish, Climate of the supercontinent Pangea. *J. Geol.* **101**, 215–233 (1993).

27. A. Donohoe, J. Marshall, D. Ferreira, D. McGee, The relationship between ITCZ location and cross-equatorial atmospheric heat transport: From the seasonal cycle to the Last Glacial Maximum. *J. Climate* **26**, 3597–3618 (2013).

28. Y.-T. Hwang, D. M. M. Frierson, Link between the double-Intertropical Convergence Zone problem and cloud biases over the Southern Ocean. *Proc. Natl. Acad. Sci. U.S.A.* **110**, 4935–4940 (2013).

29. W. Zhou, S.-P. Xie, Intermodel spread of the double-ITCZ bias in coupled GCMs tied to land surface temperature in AMIP GCMs. *Geophys. Res. Lett.* **44**, 7975–7984 (2017).

30. N. G. Loeb, D. R. Doelling, H. Wang, W. Su, C. Nguyen, J. G. Corbett, L. Liang, C. Mitrescu, F. G. Rose, S. Kato, Clouds and the Earth's radiant energy system (CERES) energy balanced and filled (EBAF) top-of-atmosphere (TOA) Edition-4.0 Data Product. *J. Climate* **31**, 895–918 (2018).

31. A. Donohoe, D. S. Battisti, Atmospheric and surface contributions to planetary albedo. *J. Climate* **24**, 4402–4418 (2011).

32. A. Jonsson, F. Bender, Persistence and variability of earth's interhemispheric albedo symmetry in 19 years of CERES EBAF observations. *J. Climate* **35**, 249–268 (2022).

33. S. Kato, F. G. Rose, D. A. Rutan, T. J. Thorsen, N. G. Loeb, D. R. Doelling, X. Huang, W. L. Smith, W. Su, S.-H. Ham, Surface irradiances of edition 4.0 clouds and the Earth's radiant energy system (CERES) energy balanced and filled (EBAF) data product. *J. Climate* **31**, 4501–4527 (2018).

34. J. Marshall, A. Donohoe, D. Ferreira, D. McGee, The ocean's role in setting the mean position of the Inter-Tropical Convergence Zone. *Clim. Dyn.* **42**, 1967–1979 (2014).

35. Y. Zheng, B. S. Giese, Ocean heat transport in Simple Ocean Data Assimilation: Structure and mechanisms. *J. Geophys. Res.* **114**, C11009 (2009).

36. R. Lumpkin, K. Speer, Global Ocean meridional overturning. *J. Phys. Oceanogr.* **37**, 2550–2562 (2007).

37. J. P. Peixoto, A. H. Oort, *Physics of Climate* (American Institute of Physics, 1992), pp. 196–206.

38. P. Cessi, The global overturning circulation. *Ann. Rev. Mar. Sci.* **11**, 249–270 (2019).

39. L. D. Talley, Shallow, intermediate, and deep overturning components of the global heat budget. *J. Phys. Oceanogr.* **33**, 530–560 (2003).

40. T. Kuhlbrodt, A. Griesel, M. Montoya, A. Levermann, M. Hofmann, S. Rahmstorf, On the driving processes of the Atlantic meridional overturning circulation. *Rev. Geophys.* **45**, RG2001 (2007).

41. M. S. Lozier, F. Li, S. Bacon, F. Bahr, A. S. Bower, S. A. Cunningham, M. F. de Jong, L. de Steur, B. deYoung, J. Fischer, S. F. Gary, B. J. W. Greenan, N. P. Holliday, A. Houk, L. Houpert, M. E. Inall, W. E. Johns, H. L. Johnson, C. Johnson, J. Karstensen, G. Koman, I. A. Le Bras, X. Lin, N. Mackay, D. P. Marshall, H. Mercier, M. Oltmanns, R. S. Pickart, A. L. Ramsey, D. Rayner, F. Straneo, V. Thierry, D. J. Torres, R. G. Williams, C. Wilson, J. Yang, I. Yashayaev, J. Zhao, A sea change in our view of overturning in the subpolar North Atlantic. *Science* **363**, 516–521 (2019).

42. I. M. Held, The Partitioning of the poleward energy transport between the tropical ocean and atmosphere. *J. Atmos. Sci.* **58**, 943–948 (2001).

43. T. Schneider, Feedback of atmosphere-ocean coupling on shifts of the Intertropical Convergence Zone. *Geophys. Res. Lett.* **44**, 11,644–11,653 (2017).

44. B. Green, J. Marshall, J.-M. Campin, The 'sticky' ITCZ: Ocean-moderated ITCZ shifts. *Clim. Dyn.* **53**, 1–19 (2019).

45. A. Gnanadesikan, A simple predictive model for the structure of the oceanic pycnocline. *Science* **283**, 2077–2079 (1999).

46. R. Hallberg, A. Gnanadesikan, The role of eddies in determining the structure and response of the wind-driven Southern Hemisphere overturning: Results from the modeling eddies in the Southern Ocean (MESO) project. *J. Phys. Oceanogr.* **36**, 2232–2252 (2006).

47. G. K. Vallis, The Buoyancy-Driven Ocean Circulation, in *Atmospheric and Oceanic Fluid Dynamics* (Cambridge Univ. Press, 2006), pp. 627–661.

48. D. J. Lunt, P. J. Valdes, A. Haywood, I. C. Rutt, Closure of the Panama Seaway during the Pliocene: Implications for climate and Northern Hemisphere glaciation. *Clim. Dyn.* **30**, 1–18 (2008).

49. Z. S. Zhang, H. J. Wang, Z. T. Guo, Transition of thermohaline circulation modes and its impact on Cenozoic climate. *Quat. Sci.* **29**, 1064–1070 (2009).

50. J.-B. Ladant, C. J. Poulsen, F. Fluteau, C. R. Tabor, K. G. MacLeod, E. E. Martin, S. J. Haynes, M. A. Rostami, Paleogeographic controls on the evolution of Late Cretaceous ocean circulation. *Clim. Past* **16**, 973–1006 (2020).

51. H. J. Yang, Q. Wen, Investigating the role of the Tibetan plateau in the formation of Atlantic meridional overturning circulation. *J. Climate* **33**, 3585–3601 (2020).

52. J. Nie, W. Boos, Z. Kuang, Observational evaluation of a convective quasi-equilibrium view of monsoons. *J. Climate* **23**, 4416–4428 (2010).

53. T. A. Shaw, O. Miyawakia, A. Donohoe, Stormier Southern Hemisphere induced by topography and ocean circulation. *Proc. Natl. Acad. Sci. U.S.A.* **119**, e2123512119 (2022).

54. J. W. Hurrell, M. M. Holland, P. Gent, S. Ghan, J. E. Kay, P. Kushner, J.-F. Lamarque, W. G. Large, D. Lawrence, K. Lindsay, W. H. Lipscomb, M. Long, N. Mahowald, D. R. Marsh, R. B. Neale, P. J. Rasch, S. J. Vavrus, M. Vertenstein, D. C. Bader, W. Collins, J. J. Hack, J. T. Kiehl, S. J. Marshall, The community earth system model: A framework for collaborative research. *Bull. Am. Meteorol. Soc.* **94**, 1339–1360 (2013).

55. C. R. Scotese, N. Wright, PALEOMAP Paleodigital Elevation Models (PaleoDEMS) for the Phanerozoic PALEOMAP Project (2018); www.earthbyte.org/paleodem-resource-scotese-and-wright-2018/.

56. C. R. Scotese, Phanerozoic Temperature Curve. PALEOMAP Project (2015); www.academia.edu/12114306/Phanerozoic_Global_Temperature_Curve.

57. C. R. Scotese, Some Thoughts on Global Climate Change: The Transition for Icehouse to Hothouse Conditions. PALEOMAP Project (2016); www.researchgate.net/publication/275277369_Some_Thoughts_on_Global_Climate_Change_The_Transition_for_Icehouse_to_Hothouse_Conditions/.

58. D. O. Gough, Solar interior structure and luminosity variations. *Sol. Phys.* **74**, 21–34 (1981).

59. R. F. Adler, G. J. Huffman, A. Chang, R. Ferraro, P. Xie, J. Janowiak, B. Rudolf, U. Schneider, S. Curtis, D. Bolvin, A. Gruber, J. Susskind, P. Arkin, The version-2 global precipitation climatology project (GPCP) monthly precipitation analysis (1979–present). *J. Hydrometeorol.* **4**, 1147–1167 (2003).

60. European Centre for Medium-Range Weather Forecasts. 2019, updated yearly. ERA5 Reanalysis (Monthly Mean 0.25 Degree Latitude-Longitude Grid). Research Data Archive at the National Center for Atmospheric Research, Computational and Information Systems Laboratory. https://doi.org/10.5065/P8GT-0R61.